Bicircular light Floquet engineering of magnetic symmetry and topolgy, and its application to Dirac semimetal Cd_3As_2

Thaís V. Trevisan,[1,2,*] Pablo Villar Arribi,[3,†] Olle Heinonen,[3] Robert-Jan Slager,[4,5] and Peter P. Orth[1,2,‡]

[1] *Ames Laboratory, Ames, Iowa 50011, USA*
[2] *Department of Physics and Astronomy, Iowa State University, Ames, Iowa 50011, USA*
[3] *Materials Science Division, Argonne National Laboratory, Lemont, Illinois 60439, USA*
[4] *TCM Group, Cavendish Laboratory, University of Cambridge, Cambridge CB3 0HE, United Kingdom*
[5] *Department of Physics, Harvard University, Cambridge MA 02138, USA*

(Dated: April 26, 2022)

We show that bicircular light (BCL) is a versatile way to control magnetic symmetries and topology in materials. The electric field of BCL, which is a superposition of two circularly polarized light waves with frequencies that are integer multiples of each other, traces out a rose pattern in the polarization plane that can be chosen to break selective symmetries, including spatial inversion. Using a realistic low-energy model, we theoretically demonstrate that the three-dimensional Dirac semimetal Cd_3As_2 is a promising platform for BCL Floquet engineering. Without strain, BCL irradiation induces a transition to a non-centrosymmetric magnetic Weyl semimetal phase with tunable energy separation between the Weyl nodes. In the presence of strain, we predict the emergence of a magnetic topological crystalline insulator with exotic unpinned surface Dirac states that are protected by a combination of twofold rotation and time-reversal ($2'$) and can be controlled by light.

Introduction.– Recent years have seen a surge of interest in symmetry-protected topological phases with unique properties arising from a nontrivial topology of the bulk band structure. Examples are topological (crystalline) insulators [1–4] with dissipationless metallic surface states, magnetic axion insulators with large magnetoelectric couplings [5–7], and three-dimensional (3D) Dirac and Weyl semimetals (SM) with exotic Fermi arc surface states [8]. Topological states also emerge in artificial systems such as cold atomic gases [9] and photonic waveguides [10]. The connection between symmetry and band topology is made explicit in classification schemes based on topological invariants like Chern and winding numbers [11], and in the more refined classification of crystalline materials using band compatibility relations [12–15], effectively generalize the parity indicator of Fu and Kane [16]. A particularly rich set of symmetry-protected topological phases arises from magnetic symmetries, which combine time-reversal (TR) with spatial symmetries, leading to a classification of phases in the 1651 magnetic space groups (MSGs) [17–19].

The relation between symmetry and topology not only facilitates the search for new realizations of symmetry-protected topological phases, but can also be employed to actively tune between different topological states by applying symmetry-breaking perturbations. Among them, periodic Floquet perturbations such as caused by irradiation with strong coherent light are particularly attractive since they allow for a *dynamic manipulation* on ultrafast time scales [20–25]. Floquet engineering of topological band structures has also been experimentally realized in artifical lattice systems [9, 26–29] and photonic systems [10, 30]. In real materials, light-control of symmetry has been achieved via a direct Floquet-dressing of electronic states using circularly polarized light (CL) [31, 32], but also via exciting resonant lattice modes [33–37], and via photocurrent generation [38]. It was experimentally shown that TR breaking via CL irradiation can induce a quantum anomalous Hall state in topological insulator (TI) surface states [31] and in graphene [32, 39].

Here, we show that Floquet engineering with bicircular light (BCL), which consists of a superposition of two CL waves with integer frequency ratio, offers an even greater tunability. The key idea is to use the polarization state of BCL to selectively break spatial symmetries, *including inversion* ($\mathcal{I}$), with direct consequences on band topology. This opens the possibility to realize non-centrosymmetric magnetic topological phases with unique, e.g., chiral and polar, properties. In two dimensions, the effect of BCL on graphene was recently discussed theoretically in Ref. 40. We here propose to use BCL to tune 3D topological semimetallic and insulating parent phases, where the presence of a nodal point in the bulk or surface spectrum is protected by symmetries. Application of BCL can lift these symmetries and induce a desired topological phase transition by imposing a particular magnetic symmetry group from one the subgroups of the crystal MSG.

We emphasize that BCL Floquet engineering is a general approach that can be applied to a wide variety of systems including solid-state materials and artificial lattices. In the following, we consider a minimal model that describes general centrosymmetric 3D Dirac SM and TIs. For concreteness and to make quantitative predictions, we consider model parameters that describes the 3D SM Cd_3As_2 [41] as an example. This material is a promising platform for BCL Floquet engineering, since high-mobility films are available [42] and the low-energy topological bands (arising from narrow As-4p states) are well separated in energy from other trivial bands by hun-

dreds of meV [43]. This avoids heating of the topological states under a suitably chosen off-resonant Floquet drive in the mid to near infrared.

Theory of BCL Floquet engineering.– BCL corresponds to the superposition of two CL waves with opposite chirality and frequencies that are an integer ratio η of each other. It is described by the vector potential

$$\mathbf{A}(t) = \mathcal{A}_0\sqrt{2}\,\mathrm{Re}\left[e^{-i(\eta\omega t-\alpha)}\boldsymbol{\varepsilon}_R + e^{-i\omega t}\boldsymbol{\varepsilon}_L\right], \quad (1)$$

where $\mathcal{A}_0$ is the amplitude and $\boldsymbol{\varepsilon}_{L/R}$ are left (L) and right (R) CL polarization basis vectors (for details see Supplemental Material [44]). We assume uniform light illumination and neglect the photon momentum as it is typically much smaller than system momenta. This vector potential, and the corresponding electric field, traces out a $(\eta+1)$-fold rose curve over a period $T = 2\pi/\omega$, as illustrated in Fig. 1(a). The spatial dependence of $\mathbf{A}(t)$ is crucial for breaking crystal symmetries that cannot be broken by CL such as spatial inversion $\mathcal{I}$. Different magnetic symmetries can be broken by tuning the BCL frequency ratio η, which sets the rose pattern shape, the relative phase α, which promotes a rotation of the pattern, and the light incidence direction. We note that experimentally changing η and α is achieved by frequency selecting a particular higher-harmonic light mode with frequency $\eta\omega$ and by modifying the phase shift α between the fundamental and the higher-harmonic mode.

We consider BCL Floquet engineering in a generic 4-band model describing centrosymmetric 3D Dirac SMs with two Dirac nodes near the Fermi level [43, 45],

$$\hat{h}(\mathbf{k}) = M_{\mathbf{k}}\sigma_0\tau_z + \varepsilon_{\mathbf{k}}\sigma_0\tau_0 + P_{\mathbf{k}}\sigma_z\tau_x - Q_{\mathbf{k}}\sigma_0\tau_y\,. \quad (2)$$

Here, σ_i, τ_i are Pauli matrices in spin and orbital space, respectively. The momentum-dependent coefficients $M_{\mathbf{k}}$ and $\varepsilon_{\mathbf{k}}$ describe spin-independent hopping processes and $P_{\mathbf{k}}$ and $Q_{\mathbf{k}}$ describe couplings between the orbital and the spin degrees of freedom. The underlying crystal symmetry enforces a certain form of the coefficients [44].

BCL couples to the system degrees of freedom via the standard Peierls' substitution, $\hat{h}[\mathbf{k}+\mathbf{A}(t)]$. Choosing an off-resonant light frequency ω that is larger than the electronic transition energies allows for the use of a high-frequency approximation [46–49]. This results in a time-independent effective Floquet-Bloch Hamiltonian

$$\hat{h}_{\mathrm{eff}}(\mathbf{k}) = \hat{h}_0(\mathbf{k}) + \hat{m}(\mathbf{k})\,, \quad (3)$$

$$\hat{m}(\mathbf{k}) = \frac{1}{\omega}\sum_{n=1}^{\infty}\frac{1}{n}\left[\hat{h}_n(\mathbf{k}), \hat{h}_{-n}(\mathbf{k})\right] + \mathcal{O}(\omega^{-2})\,. \quad (4)$$

Here, $\hat{h}_n(\mathbf{k}) = (1/T)\int_0^T dt\; e^{-in\omega t}\;\hat{h}[\mathbf{k}+\mathbf{A}(t)]$ is the n-th Fourier component of the time-dependent Hamiltonian. We discuss higher-order contributions and corrections to the high frequency regime in the Supplementary Material [44]. The two terms in Eq. (3) depend on the BCL polarization state and incidence direction, and modify the bulk energy bands. While $\hat{h}_0$, which is the time average of $\hat{h}[\mathbf{k}+\mathbf{A}(t)]$, merely shifts the position of the Dirac nodes, the light-induced mass term

$$\hat{m}(\mathbf{k}) = m_{1,\mathbf{k}}\,\sigma_z\tau_y + m_{2,\mathbf{k}}\,\sigma_0\tau_x + m_{3,\mathbf{k}}\,\sigma_z\tau_z\,, \quad (5)$$

lifts the band degeneracy and drives topological transitions. Note that $\hat{m}(\mathbf{k})$ contains Pauli matrix products that are absent in the original model. The functions $m_{j,\mathbf{k}}$ involve combinations of $\hat{h}_n(\mathbf{k})$ (see [44] for their analytical form). Although CL and BCL generate the same set of terms in Eq.(5), the momentum dependence of $m_{j,\mathbf{k}}$ is different in the two cases, leading to a distinct symmetry breaking as shown in Table I.

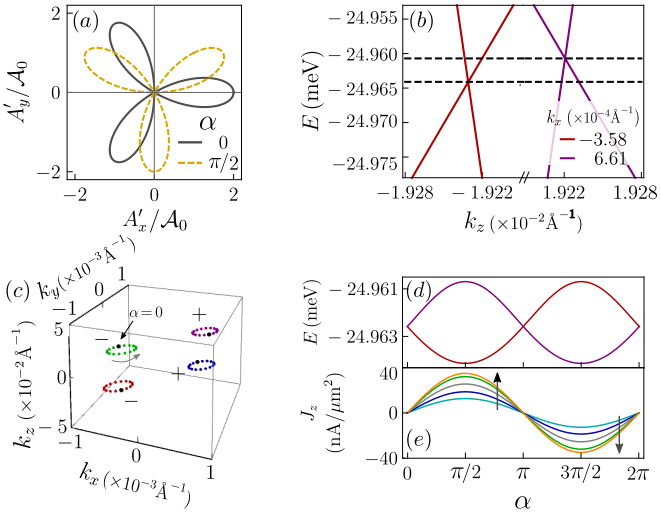

FIG. 1. BCL control of Weyl node locations in Cd_3As_2 and transport signature. (a) BCL vector potential $\mathbf{A}(t)$ for $\eta = 2$ and different α, leading to a rotation of the rose pattern. A'_x, A'_y refer to two orthogonal directions in the polarization plane. Panels (b)-(d) show the location of Weyl nodes in Cd_3As_2 as a function of α for BCL direction normal to (112) surface. (b) Cut of the bulk bands of the effective Hamiltonian in Eq. (3) for fixed $k_y = k_x$ and k_x as indicated. Here, we set $\omega = 5E_{\mathrm{Lif}} = 300$ meV, $\mathcal{A}_0 = 2.6\times10^{-2}$ Å^{-1} and $\alpha = \pi/2$. A narrow energy window is shown to emphasize the energy separation of two of the Weyl nodes (see [44] for the full spectrum). (c) Trajectory of the Weyl nodes in momentum space as α evolves from 0 (black dots) to 2π. The Weyl nodes move counterclockwise, as indicated by the gray arrow. The signs indicates the chirality of each node. Other parameters are identical to the ones in panel (b). Note the different scales on k_x, k_y and k_z axes. (d) Energy of Weyl nodes as a function of α. (e) Gyrotropic magnetic effect induced electric current as a response to a low-frequency oscillating magnetic field in the $\hat{z}$ direction as a function of α. We set the amplitude of the field to 3T. Different colors refer to distinct values of 0.02Å$^{-1} \le \mathcal{A}_0 \le 0.028$Å^{-1} with increasing steps of 0.002 Å^{-1} in the direction of the arrows.

BCL Floquet engineering of Cd_3As_2.– For concreteness, we focus in the following on a parameter set in model (2) that describes the tetragonal 3D Dirac SM

Cd_3As_2 [43, 44, 50, 51]. This material exhibits two Dirac nodes located on the k_z axis, which are protected by four-fold rotation symmetry (C_{4z}). The characteristic low energy scale describing the band inversion is given by the Lifshitz energy $E_{\rm Lif} = 60$ meV. Since trivial higher energy bands are well separated in energy, the low energy physics can be quantitatively described by a low-order expansion of the functions in Eq. (2) around $\mathbf{k} = 0$ [43, 51].

Irradiation with BCL breaks both TR and $\mathcal{I}$ symmetries and thus results in a splitting of the two Dirac nodes into four Weyl nodes. Generically, they reside at different momenta and energies [see Fig. 1(b,c)], unless the presence of additional symmetries, which relate partner Weyl nodes with opposite chirality, forces these two to lie at the same energy. For example, for BCL incident normal to (112) and $\alpha = 0$ or π, one of the arms of the rose pattern aligns with the $[1\bar{1}0]$-axis [see x-axis in Fig. 1(a)] and $m'_{[1\bar{1}0]}$ symmetry is preserved. Thus, two partner nodes connected by $m'_{[1\bar{1}0]}$ have the same energy. For all other values of α, the four nodes are separated both in energy and momentum. The energy separation between partner Weyl cones is quadratic in BCL amplitude $\mathcal{A}_0$ and scales as $1/\omega^2$. Thus, as α is varied between 0 and 2π, the Weyl nodes trace out closed loops in energy-momentum space [see Fig. 1(c)]. The size of the loop increases with the light amplitude $\mathcal{A}_0$, which opens the possibility of light-induced braiding of the Weyl nodes. While in Cd_3As_2 we found that Weyl nodes of opposite chirality annihilate before braiding occurs, such a scenario may be possible in other models with larger Lifshitz energy or with Weyl nodes in different bulk gaps. Interestingly, braiding Weyl nodes in different gaps can change their frame charge, leading to the situation that nodes with equal net frame charge reside in a given gap [52–56]. As a consequence of the emergent obstruction to the annihilation of Weyl nodes, a new invariant emerges, known as the Euler class, which is yet to be fully explored.

The dynamical manipulation of the energy separation between the Weyl nodes has another interesting consequence if one applies an additional slowly oscillating magnetic field $\mathbf{B}(t)$. According to the gyrotropic magnetic effect [57, 58], a non-centrosymmetry Weyl SM develops an electric current $\boldsymbol{J} \propto \boldsymbol{B}$ as a response, whose amplitude is also proportional to the energy difference ΔE of partner Weyl nodes: $J = \frac{e^2}{3h^2} B \Delta E$. Importantly, ΔE can be controlled by the BCL amplitude $\mathcal{A}_0$ and the relative phase parameter α. We note that this effect requires the frequency of $\mathbf{B}$ to be smaller than the scale of interband transitions, which is given by ΔE and lies in the 100 MHz range for the parameters of Fig. 1, and ultraclean samples, since the gyrotropic current is suppressed by disorder [44, 57]. In the clean limit, we predict the gyrotropic current in BCL driven Cd_3As_2 to lie within an experimentally accessible nA/μm^2 range for realistic electric field amplitudes $E_0 = \omega \mathcal{A}_0 \simeq 10^7$ V/m and a magnetic field $B \simeq 3$ T, which is modulated at less than MHz frequencies [59]. Due to the linear dispersion around the Weyl nodes, the gyrotropic magnetic effect exhibits only a weak temperature dependence, and we predict it to be robust up to 10 K [44]. As shown in Fig. 1(e), the current J is modulated as a function of α and vanishes for $\alpha = 0, \pi$, where $\Delta E = 0$. To compute J, we have set the chemical potential equal to the energy of the pair of Weyl nodes in Fig. 1(b) at $\alpha = 0$. To reveal a unique signature of bulk Weyl nodes, we propose dynamically modulating $\alpha(t)$ on a frequency scale different from that of the magnetic field (e.g., in the GHz range) in order to change the gyrotropic current at the same frequency. Importantly, even in the unavoidable presence of interband transitions and heating in real materials, which is an inherent challenge in Floquet engeneering, the coherent modulation of the gyromagnetic current can still be detected in a lock-in type experiment, since incoherent effects and heating are independent of α.

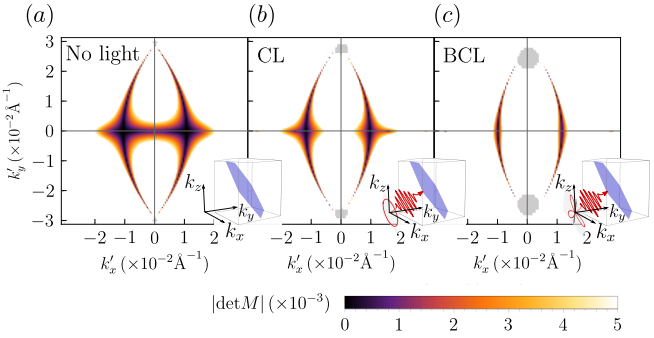

FIG. 2. Effect of CL and BCL on Fermi arc surface states at energy $E = -E_{\rm Lif}/2 = -30$ meV, the location of Dirac nodes in the absence of light, on the (112) surface of Cd_3As_2 (shown in blue in the insets). k'_x and k'_y are components of the surface momentum along directions $[1\bar{1}0]$ and $[11\bar{1}]$, respectively. The gray regions correspond to the projection of bulk states onto the surface. Different panels show surface states: (a) in the absence of light, (b) for CL with light direction normal to (112), (c) for BCL with light direction normal to (112). In (b) and (c) we set $\omega = 5E_{\rm Lif} = 300$ meV, $\mathcal{A}_0 = 2 \times 10^{-2}$Å^{-1} and $\alpha = 0$. The condition $\det M = 0$ reflects our choice of boundary condition, and can be interpreted as finite overlap to bulk states [44]. Note that the results in panel (c) depend only weakly on the value of α.

Finally, light irradiation also impacts the shape, curvature and position of the Fermi arc surface states in Cd_3As_2, which allows to manipulate surface transport properties [60]. Figure 2 shows Fermi arc surface states on the experimentally accessible (112) surface [42] at fixed energy, both without light and in the presence of CL or BCL. The geometry of the Fermi arcs, which connect projections of the nodal points onto the (112) surface, is different for CL and BCL [44].

Floquet engineering of strained Cd_3As_2.– Under the influence of lattice strain that breaks C_{4z} symmetry,

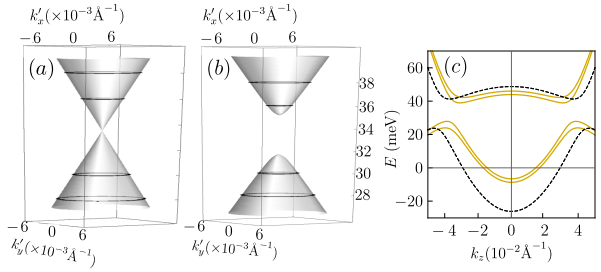

FIG. 3. CL induced topological transition from topological to axion insulator gaps out the surface states in the (001) surface of Cd_3As_2 under B_{1g} strain. Panel (a) is in the absence of light and (b) is in the presence of CL with $\omega = 5E_{\rm Lif} = 400$ meV and $\mathcal{A}_0 = 2.4\times10^{-2}$Å^{-1}, incident normal to (112), as in the inset of Fig. 2(b). Here, k'_x (k'_y) points along the [100] ([010]) direction. (c) Cut of the bulk bands of strained Cd_3As_2 for fixed $k_x = k_y = 0$ in absence (dashed) and presence (solid) of CL light with the same parameters as in panel (b).

Cd_3As_2 becomes a strong TI with gapless Dirac surface states on every crystal surface. In the following, we consider experimentally realistic types of strain: first, B_{1g}-symmetric strain that breaks C_{4z} and the two-fold rotations along the diagonals, $C_{2,[110]}$ and $C_{2,[1\bar10]}$ [42, 51]. We also consider B_{2g}-symmetric strain that breaks C_{4z} and the two-fold rotations along the crystallographic axes, $C_{2,[100]}$ and $C_{2,[010]}$. Within the generic 4-band model in Eq. (2), B_{1g} and B_{2g} strains correspond to terms of the form $B_{\mathbf{k}}\sigma_x\tau_x$ and $B_{\mathbf{k}}\sigma_y\tau_x$, respectively, where $B_{\mathbf{k}} \propto k_z$. Additional terms that renormalize the parameters in Eq. (2) are allowed by symmetry, but vanish along k_z and thus do not contribute to the size of the bulk gap. Under irradiation these strain terms lead to additional light-induced mass terms beyond those listed in Eq. (5) that also contribute to magnetic symmetry breaking (see [44]). As we show next, this opens up an interesting possibility of inducing sought-after topological states protected by magnetic symmetries. Specifically, we predict a CL-induced axion insulator state [61] and a BCL-induced magnetic topological crystalline insulator protected by $2'$ symmetry [62, 63].

Table I shows that the combination of B_{1g} strain and CL irradiation along the (112) normal removes all symmetries except $\mathcal{I}$. Since the bulk gap remains open for not too large light intensities, we can conclude that CL induces a topological transition to an axion insulator state with quantized magnetoelectric coupling and half-quantized anomalous surface Hall conductivity [5]. As $\mathcal{I}$ is naturally broken at the surface, the surface states acquire a gap as shown in Fig. 3 for the particular case of the (001) surface.

An even more intriguing situation arises in the presence of B_{2g} strain and BCL irradiation along (112) normal. Choosing α as either $\frac{\pi}{2}$ or $\frac{3\pi}{2}$ removes all symmetries except the combination of a two-fold rotation around $[1\bar10]$ and time reversal: $\Theta C_{2,[1\bar10]} \equiv 2'_{[1\bar10]}$. Since a $2'$ operation

Strain	Light type	α	MPG gen.	MSG
0	No light	×	C_{2z}, C_{4z}, C_{2y}, $\mathcal{I}$, Θ	$I4_1/acd1'$
	CL $\perp$ (112)	×	$\mathcal{I}$, $\Theta C_{2,[1\bar10]}$	$C2'/c'$
	BCL$\perp$ (112)	0, π	$\Theta M_{[1\bar10]}$	Cc'
		$\frac{\pi}{2}$, $\frac{3\pi}{2}$	$\Theta C_{2,[1\bar10]}$	$C2'$
		N.A.	1	$P1$
B_{1g}	No light	×	C_{2z}, C_{2y}, $\mathcal{I}$, Θ	$Pcca1'$
	CL$\perp$(112)	×	$\mathcal{I}$	$P\bar1$
B_{2g}	No light	×	C_{2z}, $C_{2,[110]}$, $\mathcal{I}$, Θ	$Fddd1'$
	BCL$\perp$(112)	0, π	$\Theta M_{[1\bar10]}$	Cc'
		$\frac{\pi}{2}$, $\frac{3\pi}{2}$	$\Theta C_{2,[1\bar10]}$	$C2'$
		N.A.	1	$P1$

TABLE I. Magnetic symmetries of Cd_3As_2 with and without light and lattice strain. Light incidence direction is perpendicular to the (112) surface and BCL parameter $\eta = 2$ (three-fold rose pattern). The table shows the generators of the magnetic point group (MPG) preserved by the light and the resulting MSG for Cd_3As_2. Θ refers to TR symmetry and $\mathcal{I}$ to spatial inversion. N.A. stands for none of the above. The parameter α rotates the BCL rose pattern, which controls the MSG.

reverses an odd number of spacetime coordinates (like TR and $\mathcal{I}$), the magnetoelectric coupling is still quantized [64]. Again, for light intensities that leave the bulk gap open, continuity ensures that BCL induces a topologically nontrivial axion insulator state. Here, however, not all surfaces are gapped. Instead, $(1\bar10)$ surfaces (whose surface normal is parallel to the $2'$ axis) host exotic gapless Dirac states whose nodal position is unpinned from the surface TR invariant momenta. As shown in Fig. 4, the position of the nodal point is controlled by light parameters such as frequency and intensity [44]. All other surfaces are gapped and exhibit a half-quantized anomalous surface Hall conductivity.

Conclusion.– To conclude, we show that Floquet engineering using BCL offers wide tunability of the magnetic symmetries of a system beyond the capabilities of linear or circularly polarized light. This arises from the fact that the electric field of BCL follows a rose pattern that can be tailored to break desired spatial inversion and other symmetries, in addition to time-reversal, leading to a non-centrosymmetric effective Floquet-Bloch Hamiltonian. This general approach of BCL tuning of symmetries is applicable to a wide variety of materials and artificial lattice system and can have immediate impact on their band topology. As a concrete example, we predict effects of Floquet engineering in the Dirac SM Cd_3As_2, which is a suitable material platform that undergoes various light-induced topological phase transitions. In the absence of strain, BCL leads to a non-centrosymmetric magnetic Weyl SM phase with bulk nodes separated in both energy and momentum. We demonstrate that the position of the nodes can be controlled via light parameters, opening up the possibility of braiding. In the pres-

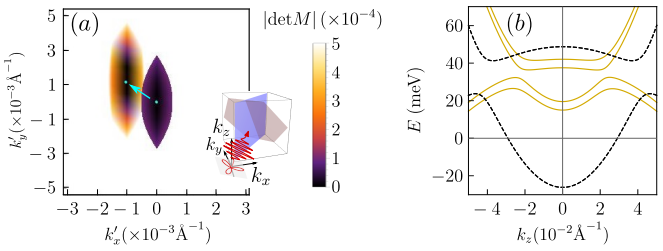

FIG. 4. BCL control of Dirac node position in light-induced 2' axion insulator state. Panel (a) shows the evolution of gapless surface states in the $(1\bar{1}0)$ surface of Cd_3As_2 (blue plane in the inset) in presence of B_{2g} strain when turning on BCL. Here, k_x' (k_y') are components along the [110] ([001]) directions. The ellipse centered around $k_x' = k_y' = 0$ is a fixed-energy cut of the surface state at 37 meV close to the node in the absence of light. BCL irradiation along direction normal to (112) (red plane in the inset) induces a $2'$ magnetic topological crystalline insulator with unpinned Dirac surface states. The surface state moves in the direction indicated by the arrow when BCL is turned on, while the energy of the Dirac node changes only slightly to 36 meV. Color shows $\det M$, which has the same meaning as in Fig. 2. (b) Bulk energy bands of strained Cd_3As_2 for fixed $k_x = k_y = 0$ without light (dashed) and with BCL (solid). In both panels, we set $\omega = 150$ meV, $\mathcal{A}_0 = 2.6 \times 10^{-2}$Å^{-1}, $\alpha = \pi/2$.

ence of an additional slowly varying magnetic field, BCL leads to a tunable dissipationless current due to the gyrotropic magnetic effect, which is a unique signature of Weyl physics. Finally, combining lattice strain and BCL irradiation realizes a sought-after magnetic axion insulator phase with exotic unpinned surface states protected by $2'$ symmetry.

We thank A. Burkov, R. McDonald, V. L. Quito, S. Stemmer and D. Yarotski for useful discussions. This research was supported by the Center for Advancement of Topological Semimetals, an Energy Frontier Research Center funded by the U.S. Department of Energy Office of Science, Office of Basic Energy Sciences, through the Ames Laboratory under Contract No. DE-AC02-07CH11358. R.-J. S. acknowledges funding from the Marie Skłodowska-Curie programme under EC Grant No. 842901 and the Winton programme as well as Trinity College at the University of Cambridge.

* thais@iastate.edu
† Present affiliation: International School for Advanced Studies (SISSA), Via Bonomea 265, I-34136 Trieste, Italy.
‡ porth@iastate.edu

[1] M. Z. Hasan and C. L. Kane, Rev. Mod. Phys. **82**, 3045 (2010).
[2] X.-L. Qi and S.-C. Zhang, Rev. Mod. Phys. **83**, 1057 (2011).
[3] L. Fu, Phys. Rev. Lett. **106**, 106802 (2011).
[4] R.-J. Slager, A. Mesaros, V. Juričić, and J. Zaanen, Nat. Phys. **9**, 98 (2012).
[5] R. S. K. Mong, A. M. Essin, and J. E. Moore, Phys. Rev. B **81**, 245209 (2010).
[6] A. M. Essin, J. E. Moore, and D. Vanderbilt, Phys. Rev. Lett. **102**, 146805 (2009).
[7] X.-L. Qi, T. L. Hughes, and S.-C. Zhang, Phys. Rev. B **78**, 195424 (2008).
[8] N. P. Armitage, E. J. Mele, and A. Vishwanath, Rev. Mod. Phys. **90**, 015001 (2018).
[9] N. R. Cooper, J. Dalibard, and I. B. Spielman, Rev. Mod. Phys. **91**, 015005 (2019).
[10] T. Ozawa, H. M. Price, A. Amo, N. Goldman, M. Hafezi, L. Lu, M. C. Rechtsman, D. Schuster, J. Simon, O. Zilberberg, and I. Carusotto, Rev. Mod. Phys. **91**, 015006 (2019).
[11] A. P. Schnyder, S. Ryu, A. Furusaki, and A. W. W. Ludwig, Phys. Rev. B **78**, 195125 (2008).
[12] J. Kruthoff, J. de Boer, J. van Wezel, C. L. Kane, and R.-J. Slager, Phys. Rev. X **7**, 041069 (2017).
[13] B. Bradlyn, L. Elcoro, J. Cano, M. G. Vergniory, Z. Wang, C. Felser, M. I. Aroyo, and B. A. Bernevig, Nature **547**, 298 (2017).
[14] A. Bouhon and A. M. Black-Schaffer, Phys. Rev. B **95**, 241101 (2017).
[15] H. C. Po, A. Vishwanath, and H. Watanabe, Nat Commun **8**, 50 (2017).
[16] L. Fu and C. L. Kane, Phys. Rev. B **76**, 045302 (2007).
[17] H. Watanabe, H. C. Po, and A. Vishwanath, Sci. Adv. **4**, eaat8685 (2018).
[18] L. Elcoro, B. J. Wieder, Z. Song, Y. Xu, B. Bradlyn, and B. A. Bernevig, Magnetic Topological Quantum Chemistry (2020), arXiv:2010.00598 [cond-mat.mes-hall].
[19] A. Bouhon, G. F. Lange, and R.-J. Slager, Phys. Rev. B **103**, 245127 (2021).
[20] T. Oka and H. Aoki, Phys. Rev. B **79**, 081406 (2009).
[21] T. Kitagawa, T. Oka, A. Brataas, L. Fu, and E. Demler, Phys. Rev. B **84**, 235108 (2011).
[22] H. Hübener, M. A. Sentef, U. De Giovannini, A. F. Kemper, and A. Rubio, Nature Communications **8**, 13940 (2017).
[23] T. Oka and S. Kitamura, Annu. Rev. Condens. Matter Phys. **10**, 387 (2019).
[24] M. S. Rudner and N. H. Lindner, Nature Reviews Physics **2**, 229 (2020).
[25] C. P. Weber, Journal of Applied Physics **129**, 070901 (2021).
[26] J. Struck, C. Ölschläger, M. Weinberg, P. Hauke, J. Simonet, A. Eckardt, M. Lewenstein, K. Sengstock, and P. Windpassinger, Phys. Rev. Lett. **108**, 225304 (2012).
[27] K. Jiménez-García, L. J. LeBlanc, R. A. Williams, M. C. Beeler, A. R. Perry, and I. B. Spielman, Phys. Rev. Lett. **108**, 225303 (2012).
[28] G. Jotzu, M. Messer, R. Desbuquois, M. Lebrat, T. Uehlinger, D. Greif, and T. Esslinger, Nature **515**, 237 (2014).
[29] C. Weitenberg and J. Simonet, Nature Physics 10.1038/s41567-021-01316-x (2021).
[30] M. C. Rechtsman, J. M. Zeuner, Y. Plotnik, Y. Lumer, D. Podolsky, F. Dreisow, S. Nolte, M. Segev, and A. Szameit, Nature **496**, 196 (2013).
[31] Y. H. Wang, H. Steinberg, P. Jarillo-Herrero, and N. Gedik, Science **342**, 453 (2013).

[32] J. W. McIver, B. Schulte, F.-U. Stein, T. Matsuyama, G. Jotzu, G. Meier, and A. Cavalleri, Nature Physics **16**, 38 (2020).

[33] M. Först, C. Manzoni, S. Kaiser, Y. Tomioka, Y. Tokura, R. Merlin, and A. Cavalleri, Nature Physics **7**, 854 (2011).

[34] E. J. Sie, C. M. Nyby, C. D. Pemmaraju, S. J. Park, X. Shen, J. Yang, M. C. Hoffmann, B. K. Ofori-Okai, R. Li, A. H. Reid, S. Weathersby, E. Mannebach, N. Finney, D. Rhodes, D. Chenet, A. Antony, L. Balicas, J. Hone, T. P. Devereaux, T. F. Heinz, X. Wang, and A. M. Lindenberg, Nature **565**, 61 (2019).

[35] A. S. Disa, M. Fechner, T. F. Nova, B. Liu, M. Först, D. Prabhakaran, P. G. Radaelli, and A. Cavalleri, Nature Physics **16**, 937 (2020).

[36] M. Y. Zhang, Z. X. Wang, Y. N. Li, L. Y. Shi, D. Wu, T. Lin, S. J. Zhang, Y. Q. Liu, Q. M. Liu, J. Wang, T. Dong, and N. L. Wang, Phys. Rev. X **9**, 021036 (2019).

[37] L. Luo, D. Cheng, B. Song, L.-L. Wang, C. Vaswani, P. M. Lozano, G. Gu, C. Huang, R. H. J. Kim, Z. Liu, J.-M. Park, Y. Yao, K. Ho, I. E. Perakis, Q. Li, and J. Wang, Nature Materials **20**, 329 (2021).

[38] N. Sirica, P. P. Orth, M. S. Scheurer, Y. M. Dai, M. C. Lee, P. Padmanabhan, L. T. Mix, S. W. Teitelbaum, M. Trigo, L. X. Zhao, G. F. Chen, B. Xu, R. Yang, B. Shen, C. C. Lee, H. Lin, T. A. Cochran, S. A. Trugman, J. X. Zhu, M. Z. Hasan, N. Ni, X. G. Qiu, A. J. Taylor, D. A. Yarotski, and R. P. Prasankumar, Photocurrent-driven transient symmetry breaking in the Weyl semimetal TaAs (2020), arXiv:2005.10308 [cond-mat.mtrl-sci].

[39] S. A. Sato, J. W. McIver, M. Nuske, P. Tang, G. Jotzu, B. Schulte, H. Hübener, U. De Giovannini, L. Mathey, M. A. Sentef, A. Cavalleri, and A. Rubio, Phys. Rev. B **99**, 214302 (2019).

[40] T. Nag, R.-J. Slager, T. Higuchi, and T. Oka, Phys. Rev. B **100**, 134301 (2019).

[41] M. N. Ali, Q. Gibson, S. Jeon, B. B. Zhou, A. Yazdani, and R. J. Cava, Inorganic chemistry **53**, 4062 (2014).

[42] T. Schumann, M. Goyal, H. Kim, and S. Stemmer, APL Materials **4**, 126110 (2016).

[43] Z. Wang, H. Weng, Q. Wu, X. Dai, and Z. Fang, Phys. Rev. B **88**, 125427 (2013).

[44] See Supplemental Material for details about the BCL setup, $k.p$ model for Cd_3As_2, technical details on surface state calculations and supplementary figures.

[45] M. Kargarian, M. Randeria, and Y.-M. Lu, Proceedings of the National Academy of Sciences **113**, 8648 (2016).

[46] T. Mikami, S. Kitamura, K. Yasuda, N. Tsuji, T. Oka, and H. Aoki, Phys. Rev. B **93**, 144307 (2016).

[47] S. Rahav, I. Gilary, and S. Fishman, Phys. Rev. A **68**, 013820 (2003).

[48] A. Eckardt and E. Anisimovas, New journal of physics **17**, 093039 (2015).

[49] M. Bukov, L. D'Alessio, and A. Polkovnikov, Advances in Physics **64**, 139 (2015).

[50] S. Jeon, B. B. Zhou, A. Gyenis, B. E. Feldman, I. Kimchi, A. C. Potter, Q. D. Gibson, R. J. Cava, A. Vishwanath, and A. Yazdani, Nature materials **13**, 851 (2014).

[51] P. Villar Arribi, J.-X. Zhu, T. Schumann, S. Stemmer, A. A. Burkov, and O. Heinonen, Phys. Rev. B **102**, 155141 (2020).

[52] J. Ahn, S. Park, and B.-J. Yang, Phys. Rev. X **9**, 021013 (2019).

[53] F. N. Ünal, A. Bouhon, and R.-J. Slager, Phys. Rev. Lett. **125**, 053601 (2020).

[54] A. Bouhon, Q. Wu, R.-J. Slager, H. Weng, O. V. Yazyev, and T. Bzdušek, Nature Physics **16**, 1137 (2020).

[55] Q. Wu, A. A. Soluyanov, and T. Bzdušek, Science **365**, 1273 (2019).

[56] B. Jiang, A. Bouhon, Z.-K. Lin, X. Zhou, B. Hou, F. Li, R.-J. Slager, and J.-H. Jiang, Nature Physics 10.1038/s41567-021-01340-x (2021).

[57] S. Zhong, J. E. Moore, and I. Souza, Phys. Rev. Lett. **116**, 077201 (2016).

[58] J. Ma and D. A. Pesin, Phys. Rev. B **92**, 235205 (2015).

[59] R. Schönemann, G. Rodriguez, D. Rickel, F. Balakirev, R. D. McDonald, J. Evans, B. Maiorov, C. Paillard, L. Bellaiche, M. B. Salamon, K. Gofryk, and M. Jaime, Magnetoelastic standing waves induced in uo_2 by microsecond magnetic field pulses (2021), arXiv:2103.08138 [cond-mat.mtrl-sci].

[60] G. Resta, S.-T. Pi, X. Wan, and S. Y. Savrasov, Phys. Rev. B **97**, 085142 (2018).

[61] A. M. Turner, Y. Zhang, R. S. K. Mong, and A. Vishwanath, Phys. Rev. B **85**, 165120 (2012).

[62] C. Fang and L. Fu, Phys. Rev. B **91**, 161105 (2015).

[63] J. Ahn, S. Park, D. Kim, Y. Kim, and B.-J. Yang, Chinese Physics B **28**, 117101 (2019).

[64] D. Vanderbilt, *Berry Phases in Electronic Structure Theory: Electric Polarization, Orbital Magnetization and Topological Insulators* (Cambridge University Press, 2018).

Supplemental Material for "Bicircular Light Floquet Engineering of Magnetic Symmetry and Topolgy and Its Application to the Dirac Semimetal Cd_3As_2"

Thaís V. Trevisan,[1,2,*] Pablo Villar Arribi,[3] Olle Heinonen,[3] Robert-Jan Slager,[4,5] and Peter P. Orth[1,2,†]

[1] *Ames Laboratory, Ames, Iowa 50011, USA*
[2] *Department of Physics and Astronomy, Iowa State University, Ames, Iowa 50011, USA*
[3] *Materials Science Division, Argonne National Laboratory, Lemont, Illinois 60439, USA*
[4] *TCM Group, Cavendish Laboratory, University of Cambridge, Cambridge CB3 0HE, United Kingdom*
[5] *Department of Physics, Harvard University, Cambridge MA 02138, USA*

(Dated: January 26, 2022)

CONTENTS

Appendix A: BCL setup

The polarization state of the BCL field,

$$\mathbf{A}(t) = \mathcal{A}_0\sqrt{2}\,\mathrm{Re}\left[e^{-i(\eta\omega t-\alpha)}\,\boldsymbol{\varepsilon}_R + e^{-i\omega t}\boldsymbol{\varepsilon}_L\right] \tag{A1}$$

is specified by its incidence direction $\hat{q}$, frequency ratio η between the two combined CL and their phase difference α. The dependence on $\hat{q}$ is encoded in the vectors $\boldsymbol{\varepsilon}_R$ and $\boldsymbol{\varepsilon}_L$ that spam the light polarization plane. Here, we make this dependence more explicit.

We choose $\hat{x}$, $\hat{y}$ and $\hat{z}$ to coincide with the Cd_3As_2 crystallographic axes $\hat{a} \equiv [100]$, $\hat{b} \equiv [010]$ and $\hat{c} = [001]$. A BCL is then incident with an angle φ with respect to the normal of the (001) surface of the material, i.e. the surface perpendicular to $\hat{z}$, as illustrated in Fig. 1(a). In this case, the incidence direction is simply $\hat{q}_0 = (0, \sin\varphi, -\cos\varphi)$, which is the same incidence direction of the CLs combined in the BCL wave. The polarization plane is spanned by the vectors $\hat{\varepsilon}_{0,1}$ and $\hat{\varepsilon}_{0,2}$. We set $\hat{\varepsilon}_{0,1} = \hat{x} = (1,0,0)$, and $\hat{\varepsilon}_{0,2} = (0, -\cos\varphi, -\sin\varphi)$ is obtained by rotating $\hat{\varepsilon}_{0,1}$ by $\pi/2$ around $\hat{q}_0$ in order to satisfy $\hat{\varepsilon}_{0,1} \times \hat{\varepsilon}_{0,2} = \hat{q}_0$ (see Fig. 1(b)).

* thais@iastate.edu

† porth@iastate.edu

A more generic incidence direction can be straightforwardly constructed from this simple case by rotating the incident plane by an angle β around $\hat{z}$, as illustrated in Fig. 1(c). In this case, we have

$$\hat{q} = R_{\hat{z}}(\beta)(0, \sin\varphi, -\cos\varphi) = (-\sin\beta\sin\varphi, \cos\beta\sin\varphi, -\cos\varphi) \ . \tag{A2}$$

$$\hat{\varepsilon}_1 = R_z(\beta)(1, 0, 0) = (\cos\beta, \sin\beta, 0) \ , \tag{A3}$$

$$\hat{\varepsilon}_2 = R_z(\beta)(0, -\cos\varphi, -\sin\varphi) = (\cos\varphi\sin\beta, -\cos\varphi\cos\beta, -\sin\varphi) \ . \tag{A4}$$

For a light circularly polarized to the right, the polarization is specified by $\boldsymbol{\varepsilon}_R = (\hat{\varepsilon}_1 - i\hat{\varepsilon}_2)/\sqrt{2}$, while the polarization state of a light circularly polarized to the left is given by $\boldsymbol{\varepsilon}_L = (\hat{\varepsilon}_1 + i\hat{\varepsilon}_2)/\sqrt{2}$. Substituting $\boldsymbol{\varepsilon}_R$ and $\boldsymbol{\varepsilon}_L$ into Eq. (A1), we can write the Cartesian components of the BCL vector potential in a compact form:

$$A_\mu(t) = \mathcal{A}_0\, c_\mu \left[\cos(\eta\omega t - \alpha) + \cos(\omega t)\right] + \mathcal{A}_0\, d_\mu \left[\sin(\eta\omega t - \alpha) - \sin(\omega t)\right] \ , \tag{A5}$$

where $\mu = x, y, z$. The coefficients c_μ and d_μ are parametrized by the two angles φ and β, as shown in Table A.

Note that a BCL perpendicular to (001) or, equivalently, parallel to $\hat{z} = [001]$ is obtained by setting $\beta = 0$ and $\varphi = \pi$. Since Cd_3As_2 is a tetragonal crystal, the correspondence between the indices for the surface (hkl) and its normal $[uvw]$ follows [1]

$$\frac{u}{h} = \frac{v}{k} = \frac{w}{l}\left(\frac{c}{a}\right)^2 \ , \tag{A6}$$

where $a = b$ and c are the lattice parameters in the xy plane and in $\hat{z}$ direction, respectively. For Cd_3As_2, $a = 12.633$Å and $c = 25.427$Å [2], but for calculations purposes we set $c = 2a$. In this case, a BCL normal to (112) is parallel to the $[221] = \hat{x} + \hat{y} + \hat{z}$ direction and, therefore, obtained by setting $\beta = -\pi/4$ and $\varphi = \arccos(-1/\sqrt{3})$.

Appendix B: k.p model for cadmium arsenide

In this appendix, we specify the form of the momentum-dependent coefficients of the k.p model shown in Eq.(2) in the main text for Cd_3As_2. We discuss both semimetallic and insulator states.

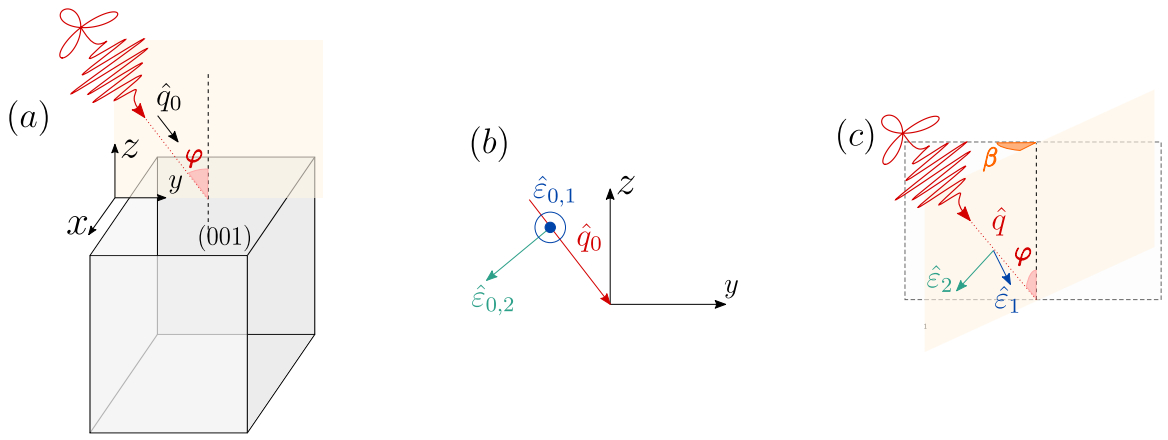

FIG. 1. (a) Illustration of the tetragonal Cd_3As_2 crystal irradiated by a BCL incident with an angle φ with respect to the normal of the (001) surface. (b) Light propagation direction $\hat{q}_0$ and vectors $\boldsymbol{\varepsilon}_1$ and $\boldsymbol{\varepsilon}_2$ defining the polarization plane for the setup shown in (a). Incidence direction and polarization vectors for a generic incidence direction.

	x	y	z
c_μ	$\cos\beta$	$\sin\beta$	0
d_μ	$-\sin\beta\cos\varphi$	$\cos\beta\cos\varphi$	$\sin\varphi$

TABLE I. Coefficients of the Cartesian components of the BCL field.

1. Semimetallic phase

Despite its complicated crystal structure, first-principle calculations show that the low energy physics of Cd_3As_2 is characterized by a minimal 4-band model [3],

$$\hat{H} = \sum_{\mathbf{k}} \hat{\psi}^{\dagger}_{\mathbf{k}} \hat{h}(\mathbf{k}) \hat{\psi}_{\mathbf{k}} \ , \tag{B1}$$

$$\hat{h}(\mathbf{k}) = M_{\mathbf{k}}\sigma_0\tau_z + P_{\mathbf{k}}\sigma_z\tau_x - Q_{\mathbf{k}}\sigma_0\tau_y + \varepsilon_{\mathbf{k}}\sigma_0\tau_0 \ . \tag{B2}$$

This model is a down-fold from an 8×8 Hamiltonian spanning the basis of Cs $5s$ and As $4p$ states where spin-orbit coupling is already accounted for locally. This Hamiltonian is diagonalized into the J basis and then a downfolded to 4-band model spanning the following basis set $\{|S_{1/2}, 1/2\rangle, |P_{3/2}, 3/2\rangle, |S_{1/2}, -1/2\rangle, |P_{3/2}, -3/2\rangle\}$. Due to the further symmetry breaks of the problem (e.g. tetragonal-orthorhombic due to strain and spatial inversion), new off-diagonal terms are included in the 4 effective Hamiltonian that mix the different states in this reduced basis set, but these off-diagonal terms are added after the diagonalization into the J-basis, leading to Eq.(B2). All these terms accounting for the different symmetry breaks in this 4-band low-energy effective model have been previously introduced by Ref. 3 and the model itself has been already used to describe surface states in Cd_3As_2 [3–5]. In Eq.(B2), $\hat{\psi}^{\dagger}_{\mathbf{k}} \equiv (c^{\dagger}_{\mathbf{k},\uparrow} d^{\dagger}_{\mathbf{k},\uparrow} c^{\dagger}_{\mathbf{k},\downarrow} d^{\dagger}_{\mathbf{k},\downarrow})$, where $c^{\dagger}_{\mathbf{k},\sigma}$ ($d^{\dagger}_{\mathbf{k},\sigma}$) creates an electron with momentum $\mathbf{k}$ and spin σ in the $5s$ ($4p$) orbital Cd (As). Besides, σ_j (τ_j), with $j = x, y, z$ are Pauli matrices in spin (orbital) space and σ_0 and τ_0 are two-by-two identity matrices. The functions preceding the Pauli matrices in Eq. (B2) are polynomials of the momentum components,

$$M_{\mathbf{k}} = M_0 - M_1 k_z^2 - M_2 \left(k_x^2 + k_y^2\right) \ , \tag{B3}$$

$$P_{\mathbf{k}} = A k_x \ , \tag{B4}$$

$$Q_{\mathbf{k}} = A k_y \ , \tag{B5}$$

$$\varepsilon_{\mathbf{k}} = C_0 + C_1 k_z^2 + C_2 \left(k_x^2 + k_y^2\right) \ . \tag{B6}$$

with coefficients calculated in Ref. [4] and summarized in Table II. Such a simple $k.p$ model is able to capture the two Dirac cones in the band structure of Cd_3As_2 because they occur in the vicinity of the Γ point ($\mathbf{k} = 0$) of the Brillouin zone, as shown in Fig. 2. The separation between the valence and conduction band at the center of the Brillouin zone gives the the Lifshitz energy $E_{Lif} = 60$ meV. The Lifshitz energy corresponds to the energy scale over which the shape of the Fermi surface changes from a single pocket to two separate pockets and later back to a single pocket.

It is important to note that terms such as Eqs. (B4) and (B5) originate from $\sin(ak_x)$ and $\sin(ak_y)$, respectively, in the tight-biding model valid in the entire Brillouin zone expanded to linear order in momentum. We noticed, however, that when light is coupled to the electrons, we need to carry the expansion at least up to third order in momentum for the symmetries of the Floquet Hamiltonian to be consistent with those preserved by the light vector potential. Accordingly, we add corrections γk_x^3 and γk_y^3 to Eq. (B4) and Eq. (B5), respectively. Symmetry allows for the coefficients of the linear and cubic terms in Eq. (B4) and Eq. (B5) to be different, and we choose $\gamma = A/6$ to ensure that the new cubic terms are only a small correction to the original expressions. Similarly, for linear terms in k_z that will appear later in the presence of strain, we add a correction four times larger ($4\gamma k_z$, with $\gamma = B_1/6$ - see Eq. (B8)) to reflect $c = 2a$.

Parameters	Semimetallic	Insulating
M_0 (eV)	0.0282	0.0374
M_1 (eV Å^2)	20.72	20.36
M_2 (eV Å^2)	13.32	18.77
C_0 (eV)	-0.0475	0.0113
C_1 (eV Å^2)	12.50	12.05
C_2 (eV Å^2)	13.62	13.13
A (eVÅ)	1.116	1.089
B_1 (eVÅ)	0	0.2566

TABLE II. Parameters for the $k.p$ model for Cd_3As_2 in both semimetallic (Dirac semimetal) and insulating (strong TI) phases. Values taken from Ref. [4]. Note that in Ref. [4] M_1 and M_2 are defined with a global minus sign. Here, we incorporated it directly in Eqs. (B3) and that is why M_1 and M_2 are positive in our table.

2. Insulating phase

The effects of strain in the plane perpendicular to $\hat{z}$ are incorporated in the $k.p$ model by adding extra terms to Eq. (B2) that break the desired symmetries. The values of the coefficient in the polynomial functions changes (see Table II), and so does the Lifshitz energy, which becomes $E_{Lif} = 80$ meV. The form of the symmetry-breaking terms depend on the type of strain we consider.

Let's start with strain type B_{1g} introduced in Ref. 4. It breaks the two-fold rotations around the diagonals in the xy plane $C_{2,[110]}$ and $C_{2,[1\bar{1}0]}$ (and the corresponding mirrors $M_{[110]}$ and $M_{[1\bar{1}0]}$) in addition to C_{4z}. All other symmetries of the unstained material remain unchanged and, as a consequence, Cd_3As_2 with B_{1g} strain is characterized by the space group $Pcca$ (No. 54). Time-reversal is also preserved in the absence of light and the corresponding magnetic space group is the grey group $Pcca1'$ (No.54.337). The generic first-quantized Hamiltonian that preserves the symmetries of this group is given by

$$\hat{h}_{B_{1g}}(\mathbf{k}) = M_{\mathbf{k}}\sigma_0\tau_z + B_{\mathbf{k}}\sigma_x\tau_x + P_{\mathbf{k}}\sigma_z\tau_x - Q_{\mathbf{k}}\sigma_0\tau_y + \varepsilon_{\mathbf{k}}\sigma_0\tau_0 \ , \tag{B7}$$

with [4]

$$B_{\mathbf{k}} = B_1\left(k_z + \frac{2k_z^3}{3}\right) \ . \tag{B8}$$

The functions $M_{\mathbf{k}}$, $P_{\mathbf{k}}$, $Q_{\mathbf{k}}$ and $\varepsilon_{\mathbf{k}}$ have the same form as in the semimetallic case, but with different coefficients (see Table II).

Strain of type B_{2g} in the xy plane, on the other hand, breaks, besides C_{4z}, the two-fold rotations around the crystallographic axes $C_{2,x}$ and $C_{2,y}$, as well as their corresponding mirrors, but preserves $C_{2,[110]}$ and $C_{2,[1\bar{1}0]}$. The resulting space group is $Fddd$ (No. 70). The first-quantized $k.p$ Hamiltonian with all the terms allowed by the symmetries of this group was obtained using python Qsymm [6] and reads

$$\hat{h}_{B_{2g}}(\mathbf{k}) = \tilde{M}_{\mathbf{k}}\sigma_0\tau_z + B_{\mathbf{k}}\sigma_y\tau_x + \tilde{P}_{\mathbf{k}}\sigma_z\tau_x - \tilde{Q}_{\mathbf{k}}\sigma_0\tau_y + \tilde{\varepsilon}_{\mathbf{k}}\sigma_0\tau_0 \ , \tag{B9}$$

where

$$\tilde{M}_{\mathbf{k}} = M_{\mathbf{k}} + s_A k_x k_y \ , \tag{B10}$$

$$\tilde{P}_{\mathbf{k}} = P_{\mathbf{k}} + \tilde{A}k_y\left(1 + \frac{k_y^2}{6}\right) \ , \tag{B11}$$

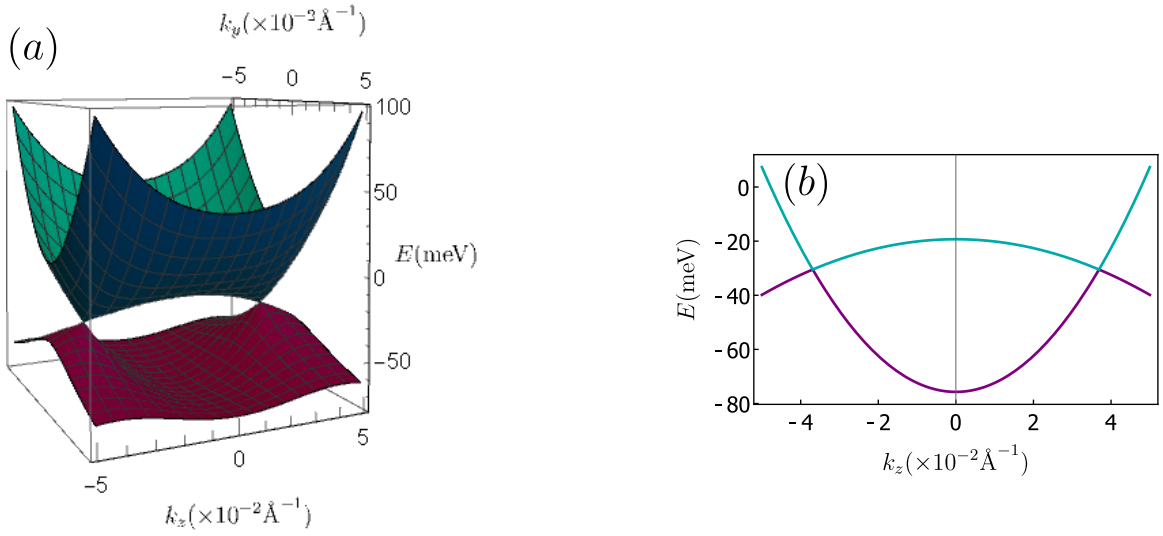

FIG. 2. Bulk bands of the $k.p$ model for Cd_3As_2 in the absence of strain and light [Eq.(B2)]. We set (a) $k_x = 0$ and (b) $k_x = k_y = 0$.

$$\tilde{Q}_{\mathbf{k}} = Q_{\mathbf{k}} + \tilde{A}k_x\left(1+\frac{k_y^x}{6}\right) \ , \tag{B12}$$

$$\tilde{\varepsilon}_{\mathbf{k}} = \varepsilon_{\mathbf{k}} + s_B k_x k_y \ , \tag{B13}$$

and $M(\mathbf{k})$, $P(\mathbf{k})$, $Q(\mathbf{k})$, $\varepsilon(\mathbf{k})$ and $B(\mathbf{k})$ defined in Eqs. (B3)-(B6) and Eq. (B8), respectively. For simplicity, we set, for simplicity, $s_A = s_B = \tilde{A} = B_1 = 0.2566$ eVÅ.

Appendix C: Light-induced mass terms

Here, we show the expressions for the light-induced mass terms $\hat{m}(\mathbf{k})$ defined in the main text. Standard high-frequency expansion [7–10] tell us that a time-independent effective Hamiltonian $\hat{H}_{eff}$ can be derived from a generic periodic Hamiltonian $\hat{H}(t) = \hat{H}(t+T)$ using

$$\hat{H}_{eff} = \hat{H}_0 + \frac{1}{\omega}\sum_{n=1}^{\infty}\frac{1}{n}\left[\hat{H}_n, \hat{H}_{-n}\right] + \mathcal{O}\left(\frac{1}{\omega^2}\right) \ , \tag{C1}$$

where

$$\hat{H}_n = \frac{1}{T}\int_0^T dt e^{-in\omega t}\hat{H}(t) \ , \tag{C2}$$

denotes the Fourier components of $\hat{H}(t)$ (with $n = 0, 1, 2, \cdots$). For the particular case of the many-body Hamiltonian Eq. (B1)), the fermionic anti-commutation relation gives

$$\hat{H}_{eff} = \sum_{\mathbf{k}} \hat{\psi}^{\dagger}_{\mathbf{k}}\, \hat{h}_{eff}(\mathbf{k})\, \hat{\psi}_{\mathbf{k}} \ , \tag{C3}$$

with

$$\hat{h}_{eff}(\mathbf{k}) = \hat{h}_0(\mathbf{k}) + \hat{m}(\mathbf{k}) \ , \tag{C4}$$

$$\hat{m}(\mathbf{k}) = \frac{1}{\omega}\sum_{n=1}^{\infty}\frac{1}{n}\left[\hat{h}_n(\mathbf{k}), \hat{h}_{-n}(\mathbf{k})\right] \ , \tag{C5}$$

as defined in the main text. Note that $\hat{h}_n(\mathbf{k})$ has the same form of the first-quantized Hamiltonian in Eq. (B2) (or Eq. (B7), or Eq. (B9) depending on which phase of Cd_3As_2 we are considering), but the functions preceding the Pauli matrices are replaced by their Fourier component after minimal coupling. For instance, $M(\mathbf{k}) \to M_n(\mathbf{k}) = (1/T)\int_0^T e^{-in\omega t}M(\mathbf{k}+\mathbf{A}(t))$. Note that $\hat{h}_0(\mathbf{k})$ is the time-average of the time-dependent first-quantized Hamiltonian $\hat{h}(\mathbf{k}+\mathbf{A}(t))$.

The term proportional to $1/\omega$ in $\hat{h}_{eff}(\mathbf{k})$ [Eq. (C5)], acts as a mass term in the location of the Dirac nodes of the unperturbed band structure and, therefore, we call it *light-induced mass term*. It has nine distinct contributions as a result of the commutations of the Pauli matrices:

$$\begin{aligned}\hat{m}(\mathbf{k}) = {} & m_{1,\mathbf{k}}\,\sigma_z\tau_y + m_{2,\mathbf{k}}\,\sigma_0\tau_x + m_{3,\mathbf{k}}\,\sigma_z\tau_z + m_{4,\mathbf{k}}\,\sigma_x\tau_y + m_{5,\mathbf{k}}\,\sigma_y\tau_0 \\ & + m_{6,\mathbf{k}}\,\sigma_x\tau_z + m_{7,\mathbf{k}}\,\sigma_y\tau_y + m_{8,\mathbf{k}}\,\sigma_x\tau_0 + m_{9,\mathbf{k}}\,\sigma_y\tau_z \ .\end{aligned} \tag{C6}$$

$m_{3,\mathbf{k}}$, $m_{4,\mathbf{k}}$ and $m_{9,\mathbf{k}}$ are always present (both semimetallic and insulating phases) and are given by

$$m_{1,\mathbf{k}} = \frac{2i}{\omega}\sum_{n=1}^{\infty}\frac{1}{n}\left(M_{n,\mathbf{k}}P_{-n,\mathbf{k}} - M_{-n,\mathbf{k}}P_{n,\mathbf{k}}\right) \ , \tag{C7}$$

$$m_{2,\mathbf{k}} = \frac{2i}{\omega}\sum_{n=1}^{\infty}\frac{1}{n}\left(M_{n,\mathbf{k}}Q_{-n,\mathbf{k}} - M_{-n,\mathbf{k}}Q_{n,\mathbf{k}}\right) \ , \tag{C8}$$

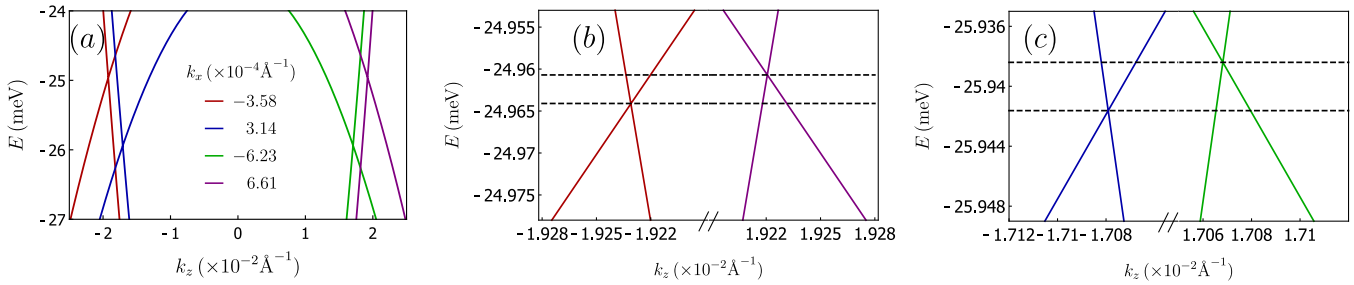

FIG. 3. (a) Cuts with $k_x = k_y$ of the bulk bands of Cd_3As_2 irradiated with BCL. We set the incidence direction normal to (112) surface, $\omega = 300\,\text{meV}$, $\mathcal{A}_0 = 2.6 \times 10^{-2}$ Å^{-1} and $\alpha = \pi/2$. Panels (b) and (c) are zooms of panels (a) to highlight the energy separation of the cones.

$$m_{3,\mathbf{k}} = -\frac{2i}{\omega}\sum_{n=1}^{\infty}\frac{1}{n}\left(P_{n,\mathbf{k}}Q_{-n,\mathbf{k}} - P_{-n,\mathbf{k}}Q_{n,\mathbf{k}}\right) \ . \tag{C9}$$

On the other hand, $m_{4,\mathbf{k}}$, $m_{5,\mathbf{k}}$ and $m_{6,\mathbf{k}}$ only exist in strained Cd_3As_2 with B_{1g}-type strain. They take the forms

$$m_{4,\mathbf{k}} = \frac{2i}{\omega}\sum_{n=1}^{\infty}\frac{1}{n}\left(M_{n,\mathbf{k}}B_{-n,\mathbf{k}} - M_{-n,\mathbf{k}}B_{n,\mathbf{k}}\right) \ , \tag{C10}$$

$$m_{5,\mathbf{k}} = -\frac{2i}{\omega}\sum_{n=1}^{\infty}\frac{1}{n}\left(B_{n,\mathbf{k}}P_{-n,\mathbf{k}} - B_{-n,\mathbf{k}}P_{n,\mathbf{k}}\right) \ , \tag{C11}$$

$$m_{6,\mathbf{k}} = -\frac{2i}{\omega}\sum_{n=1}^{\infty}\frac{1}{n}\left(B_{n,\mathbf{k}}Q_{-n,\mathbf{k}} - B_{-n,\mathbf{k}}Q_{n,\mathbf{k}}\right) \ . \tag{C12}$$

Lastly, $m_{7,\mathbf{k}}$, $m_{8,\mathbf{k}}$ and $m_{9,\mathbf{k}}$ are only present if strain of type B_{2g} is applied. They have the same form as $m_{4,\mathbf{k}}$, $-m_{5,\mathbf{k}}$ and $m_{6,\mathbf{k}}$, respectively, but with $M_{n,\mathbf{k}}$, $P_{n,\mathbf{k}}$ and $Q_{n,\mathbf{k}}$ replaced by $\tilde{M}_{n,\mathbf{k}}$, $\tilde{P}_{n,\mathbf{k}}$ and $\tilde{Q}_{n,\mathbf{k}}$.

In general, both $h_0(\mathbf{k})$ and the light-induced mass terms break symmetries of the bare Hamiltonian, but, ultimately, the latter plays a significant role in the topological transitions. That is because only $\mathbf{k}$ is able to lift the two-fold degeneracy of the bulk bands of the bare Hamiltonian. $h_0(\mathbf{k})$ only shifts the position of the original Dirac nodes.

The spectrum of the effective Hamiltonian obtained with a three-fold BCL incident perpendicular to the (112) surface of Cd_3As_2 is shown in Fig. 3 (a). Because of the simultaneous break of inversion and time-reversal symmetries, the Weyl cones are separated in momentum and energy as highlighted in 3 (b) and (c).

Both CL and BCL generate the same combination of Pauli matrices, as shown in see Eq.(C6). The difference between these two types of light is manifested in the momentum-dependence of $m_j(\mathbf{k})$. The functional form of these functions depends on the polarization state and incidence direction of the light. Therefore, the same term can break distinct symmetries in the CL and BCL cases. As an example, $m_{1(\mathbf{k})}$, preserves π rotation around the $\hat{z}$axis ($C_{2,z}$) for a single single CL, but this symmetry is broken by the same mass-term in the BCL case. In the table III, we contrast the symmetries preserved by each $m_{j,\mathbf{k}}$ generated in the absence of strain by a CL and by a BCL. In this table, both

Mass term	CL	BCL
$m_{1,\mathbf{k}}$	C_{2z}, $\mathcal{I}$, M_z, ΘC_{2x}, ΘC_{2y}, ΘM_x, ΘM_y	M_z, ΘC_{2y}, ΘM_x
$m_{2,\mathbf{k}}$	C_{2z}, $\mathcal{I}$, M_z, ΘC_{2x}, ΘC_{2y}, ΘM_x, ΘM_y	M_z, ΘC_{2y}, ΘM_x
$m_{3,\mathbf{k}}$	C_{2z}, C_{2z}, C_{4z}^{+}, C_{4z}^{-}, $\mathcal{I}$, M_z, $\mathcal{I}C_{4z}^{+}$, $\mathcal{I}C_{4z}^{-}$,ΘC_{2x}, ΘC_{2y} $\Theta C_{2,[110]}$, $\Theta C_{2x,[1\bar{1}0]}$, ΘM_x, ΘM_y, $\Theta M_{[110]}$, $\Theta M_{[1\bar{1}0]}$	M_z, ΘC_{2y}, ΘM_x

TABLE III. Symmetries of the original D_{4h} point group (plus time-reversal Θ) that is preserved by each of the mass terms induced by a CL incident parallel to $\hat{z}$ and by a BCL with and the same incidence direction and $\alpha = 0$. Here we focus in the semimetallic case, where no strain is applied to the system. Θ refers to TR symmetry and $\mathcal{I}$ to spatial inversion.

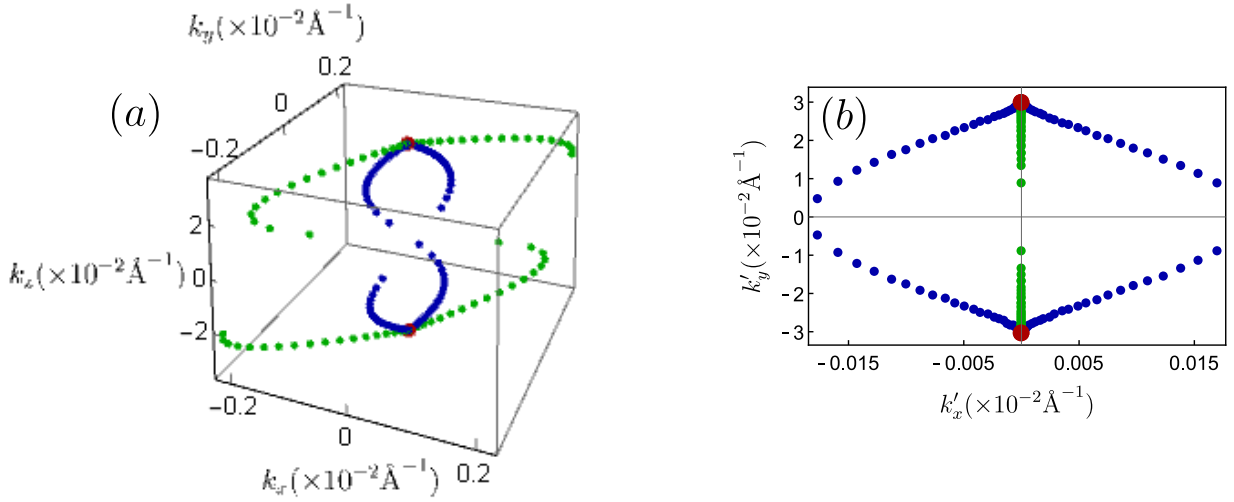

FIG. 4. (a) Evolution of the position of the Weyl nodes, in momentum space, as a function of the light amplitude ($\mathcal{A}_0$) when Cd_3As_2 is irradiated with (i) a CL light (green points) normal to the (112) surface with $0 \leq \mathcal{A}_0 \leq 3.8 \times 10^{-2}$Å^{-1} and (ii) BCL (blue points) normal to the (112) surface with $0 \leq \mathcal{A}_0 \leq 2.9 \times 10^{-2}$Å^{-1} and $\alpha = 0$. In both cases, we set $\omega = 300$ meV. Besides, the red points denote the positions of the original Dirac nodes (in the absence of light). Panel (b) shows the projections of the points of panel (a) in the (112) surface

types of light have incidence direction $\hat{z}$.

Appendix D: Controlling the position of the Weyl nodes

Both the amplitude of the light $\mathcal{A}_0$ (both BCL and CL) and the relative phase of the BCL α controls the position of the light-induced Weyl nodes. The effect of α is shown in Fig.1 (c) in the main text. Here, to further illustrate the differences between CL and BCL, we show in Fig.4 (a) the trajectory in momentum space of the Weyl nodes induced by a CL (green dots) and BCL (blue dots) as a function of $\mathcal{A}_0$. Here, both CL and BCL are incident normal to the (112) surface of Cd_3As_2 and we set $\alpha = 0$. Fig.4 (b) is a projection of Fig.4 (a) in the (112) surface.

Appendix E: Higher-order terms in the effective Hamiltonian

Terms of order $1/\omega^2$ or higher in the effective time-independent Hamiltonian in Eq.(C4) involves nested commutators of $\hat{h}_n(\mathbf{k})$. In particular, the second-order term reads

$$\hat{h}^{(2)}(\mathbf{k}) = \frac{1}{2\omega^2}\left(s_1(\mathbf{k}) + s_2(\mathbf{k})\right) \ , \tag{E1}$$

with

$$s_1(\mathbf{k}) = \sum_{n=1}^{\infty} \frac{1}{n^2}\left(\left[\left[\hat{h}_n, \hat{h}_0\right], \hat{h}_{-n}\right] + \text{h.c.}\right) \ , \tag{E2}$$

$$s_2(\mathbf{k}) = \frac{2}{3}\sum_{n,n'=1}^{\infty} \frac{1}{nn'}\left(\left[\hat{h}_n, \left[\hat{h}_{n'}, \hat{h}_{-n-n'}\right]\right] - 2\left[\hat{h}_n, \left[\hat{h}_{-n'}, \hat{h}_{n'-n}\right]\right] + \text{h.c.}\right) \ . \tag{E3}$$

Importantly, these nested commutators form a closed group. We already saw that for $\hat{h}_n(\mathbf{k})$ composed by a linear combination of $\sigma_0\tau_z$, $\sigma_x\tau_x$, $\sigma_y\tau_x$, $\sigma_z\tau_x$, $\sigma_0\tau_y$ and $\sigma_0\tau_0$, the commutator of the type $\left[\hat{h}_n, \hat{h}_m\right]$ yields the nine possible Kronecker products of Pauli matrices shown in Eq.(C6). The next order commutator $\left[\left[\hat{h}_n, \hat{h}_m\right], \hat{h}_l\right]$ accompanying terms proportional to $1/\omega^2$ produces exactly the same Pauli matrices in $\hat{h}_n(\mathbf{k})$ and, therefore, only dresses $\hat{h}_0(\mathbf{k})$. This structure repeats for higher-order commutators and we conclude that the corrections of order $\mathcal{O}(1/\omega^\alpha)$, with α,

even dresses $\hat{h}_0(\mathbf{k})$ and contribute to the shift of the original Dirac nodes (in the semi-metallic phase. For *odd* α, on the other hand, dresses $\hat{m}(\mathbf{k})$ and contribute to the momentum and energy split of the Weyl nodes. These corrections, however, are very small in the limit that $\omega > E_{Lif}$ (Lifshitz energy). Indeed, in the next section we show that the first order perturbation theory in Eqs.(C4) and (C5) reproduces accurately the Floquet quasienergies for the values of light frequencies we used in this manuscript.

Appendix F: Validity of the high-frequency expansion

In Sec.E, we saw that higher-order terms in the high-frequency expansion come with powers of $1/\omega^n$, which becomes very small when $\omega > E_{Lif}$ justifying the truncation of the effective Hamiltonian in first-order in ω. A complementary way to show the validity of this approximation is to calculate the Floquet quasienergies and compare them with the bulk bands of the effective Hamiltonian defined in Eq.(C4).

The Floquet quasienergies the eigenvalues of the Floquet Hamiltonian, which matrices alements are given by [7]

$$(H_F)_{m,n} = \frac{1}{T}\int_0^T dt\, e^{i(m-n)\omega t}\hat{h}(\mathbf{k}+\mathbf{A}(t)) - m\omega\delta_{m,n} = \hat{h}_{n-m}(\mathbf{k}) - m\omega\delta_{m,n}\ . \tag{F1}$$

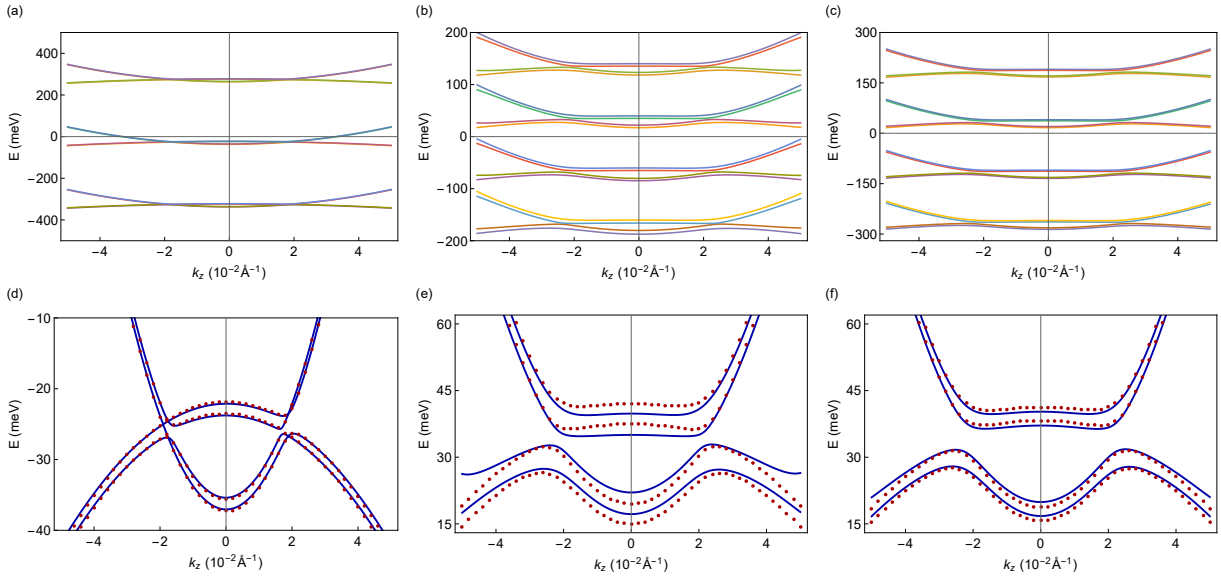

FIG. 5. Floquet quasienergies obtained for the minimal model for Cd_3As_2 irradiated with BCL normal to (112) with frequencies (a) $\omega = 300$ meV, (b) $\omega = 100$ meV and (c) $\omega = 150$ meV. In (b) and (c), BCL is combined with B_{2g}-type strain. Panels (d)-(f) correspond to the quasi-energies of (a)-(c) in the zero-photon sector (solid lines) overlaid to the band dispersion of the effective Hamiltonian obtained through high-frequency expansion (dots). In all panels, the BCL relative phase and amplitude are set to $\alpha = \pi/2$ and $\mathcal{A}_0 = 2.6 \times 10^{-2}$Å^{-1}, respectively.

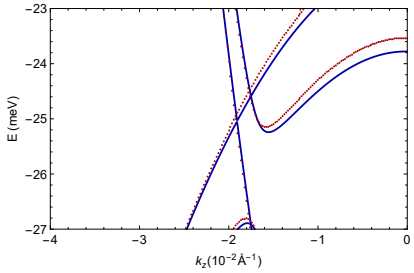

FIG. 6. Zoom of the quasienergies and effective Hamiltonian dispersion around the Weyl cone shown in Fig.6(a).

Here, $\hat{h}(\mathbf{k})$ is the first-quantized Hamiltonian defined in Eq.(B2) (or Eqs.(B7) and (B9) in the presence of strain) and $\hat{h}_n(\mathbf{k})$ represents its Fourier coefficient as defined in Eq.(C2).

Exact diagonalization of the Floquet Hamiltonian for the same values of the light parameters adopted in the main text yields a quasienergy spectrum where the different photon sectors are well separated in energy [see Fig.5 (a)-(c)]. Furthermore, for the range in momentum space where the k.p model for Cd_3As_2 holds, there is no hybridization between different photon sectors as long as $\omega > E_{Lif}$, as expected.

Figs.5 (d)-(f) are zooms of Figs.5 (a)-(c), respectively, in the zero-photon sector. In each panel, the eigenvalues effective Hamiltonian defined in Eq.(C4) (dots) are overlaid to the quasienergies (solid lines). We obtain an excellent agreement between them for $\omega > E_{Lif}$, as shown in Figs.5(d). A zoom around the Weyl node in 5(d) shows only a small quantitative difference, of order of 10^{-4}Å^{-1} in the position of the node obtained trough exact diagonalization in comparison with the high-frequency expansion [see Fig.6].

As the light frequency becomes comparable with the Lifshitz energy, however, quantitative differences emerges. This can be seen in Fig.5, where $\omega = 100$ meV and $E_{Lif} = 80$ meV. Even in this case, the frequency is still larger enough such that hybridization of quasienergies in different Floquet sectors are absent around the center of the Brilloiun zone.

Fig.5 (a) and (d) was obtained using the same parameters as in Fig.1 (b) of the main text. The remaining panels were obtained with the parameters used in Fig.4 of the main text with $\omega = 100$ meV (b) and (e) and $\omega = 150$ meV in (c) and (f). We checked that an excellent agreement between exact diagonalization of the Floquet Hamiltonian and high-frequency expansion up to $\mathcal{O}(1/\omega)$ holds for all choices of parameters in the main text.

Appendix G: Surface states

Here, we detail the method we used to calculate the surface states (SS) shown in the main text. In the following, we define two coordinate systems: (x, y, z) denotes the material frame of reference, where the $\hat{x}$ $\hat{y}$ and $\hat{z}$ are parallel to the crystallographic axes [100], [010] and [001], respectively. Since we are dealing with a tetragonal crystal, $\hat{k_x}$, $\hat{k_y}$ and $\hat{k_z}$ are also aligned with [100], [010] and [001]. The laboratory frame of reference, on the other hand, is given by (x', y', z'). The momentum components in the laboratory frame are k'_x, k'_y, and k'_z. As we will shortly see, (x, y, z) and (x', y', z') are related by a unitary transformation that depends on which material surface we want to probe for SS.

We calculate the SS by searching for evanescent states at the $z' = 0$ termination of a semi-infinite slab of Cd_3As_2 defined in the $z' < 0$ region. Instead of writing a tight-biding model with open boundaries along z' (x' and y') and solving for the surface states, here, we calculate them directly from the $k.p$ model. We use an approach similar to Ref. [4]. Evanescent states at $z' = 0$ have to fulfill two conditions: (i) $\psi_{\mathbf{k}'}(z' = 0) = 0$ and (ii) $\psi_{\mathbf{k}'}(z' \to -\infty) = 0$, where $\psi_{\mathbf{k}'}(\mathbf{r}') = u_{\mathbf{k}'}(\mathbf{r}')e^{i\mathbf{k}'\cdot\mathbf{r}'}$ are the Block wave-functions and $u_{\mathbf{k}'}(\mathbf{r}')$ are eigenstates of the first-quantized Hamiltonian $\hat{h}(\hat{U}^{-1}_{(hkl)}\mathbf{k}')$. Here, $\hat{h}(\mathbf{k})$ refer to either the bare first-quantized Hamiltonian [Eq. (B2), Eq. (B7) or Eq. (B9)] if light is absent, or to the effective first-quantized Floquet Hamiltonian [Eq. (C4)] if light is taken into account. The matrix $\hat{U}_{(hkl)}$ is the unitary transformation that aligns the normal to crystal surface labeled by the Miller indices (hkl) with $\hat{z}'$. As an example, let's say that we want to calculate the SS at the (112) surface. The normal to such surface points at the direction $[1, 1, \frac{1}{2}] = a(\hat{x} + \hat{y}) + \frac{c}{2}\hat{z} = a(\hat{x} + \hat{y} + \hat{z})$, and therefore, $\hat{z}' = (\hat{x} + \hat{y} + \hat{z})/\sqrt{3}$. Besides, the two orthogonal direction in the (112), $[1\bar{1}0] = a(\hat{x} - \hat{y})$ and $[11\bar{1}] = a(\hat{x} + \hat{y} - 2\hat{z})$, determine the x' and y' axes. This give us the transformation relation between laboratory and material frames of reference, $\mathbf{r}' = \hat{U}_{(112)}\mathbf{r}$ (and, equivalently $\mathbf{k}' = \hat{U}_{(112)}\mathbf{k}$), where

$$\hat{U}_{(112)} = \begin{pmatrix} 1/\sqrt{2} & -1/\sqrt{2} & 0 \\ 1/\sqrt{6} & 1/\sqrt{6} & -2/\sqrt{6} \\ 1/\sqrt{3} & 1/\sqrt{3} & 1/\sqrt{3} \end{pmatrix} . \tag{G1}$$

Similarly, for the $(1\bar{1}0)$ considered in the main text,

$$\hat{U}_{(1\bar{1}0)} \equiv \begin{pmatrix} 1/\sqrt{2} & 1/\sqrt{2} & 0 \\ 0 & 0 & 1 \\ 1/\sqrt{2} & -1/\sqrt{2} & 0 \end{pmatrix} . \tag{G2}$$

Condition (ii) above is satisfied for complex k'_z with a negative imaginary part $\kappa < 0$. For each point in the surface Brillouin Zone (k'_x, k'_y) and for a fixed energy E, we look for the set of complex k'_z that are solutions of the

characteristic polynomial

$$\det\left(\hat{h}(\hat{U}_{hkl}^{-1}\mathbf{k}') - E\mathbb{1}\right) = 0\ , \tag{G3}$$

and select only those with $\kappa < 0$. Besides, only solutions with κ that differ by more than a numerical precision of 10^{-5} are chosen. Not all of these complex k'_z solutions gives rise to true eigenstates of the Hamiltonian. Therefore, we substitute each of the solutions back in $\hat{h}(\hat{U}_{(hkl)}^{-1}\mathbf{k}')$ calculate its eigenvalues and eigenvectors. The eigenvectors whose eigenvalue matches the initial energy cut E correspond to localized states that decay exponentially in the region $z' < 0$. To obtain the SS, the condition $\psi_{\mathbf{k}'}(z'=0) = 0$ still needs to be fulfilled, and this is done by linear combinations of the eigenvectors just collected, which we hereafter denote by

$$\{\left|u_{\mathbf{k}'_1}\right\rangle, \left|u_{\mathbf{k}'_2}\right\rangle, \cdots\}\ . \tag{G4}$$

Note that since the coefficients of Eq. (G3) are real, its solution comes in complex conjugated pairs. Therefore, the maximum number of vectors in the set (G4) is half of the order of Eq. (G3).

A linear combination of the Block wave-functions, at $z' = 0$, constructed with the elements of Eq. (G4)

$$\phi(z'=0) = \sum_i \alpha_i u_{\mathbf{k}',i}(0)\ , \tag{G5}$$

fulfills the condition $\phi(z'=0) = 0$ if the determinant of the matrix M whose columns are the $\left|u_{\mathbf{k}'_i}\right\rangle$ entering in Eq. (G5) is zero. In this case, a SS with energy E exists at (k'_x, k'_y). Small deviations from zero means that the surface state does not exactly vanish at $z' = 0$, but its amplitude is small. We accept results states with $|detM| \leq 5 \times 10^{-3}$. This analysis is applied to all points a the grid $-0.05\text{Å}^{-1} \leq k'_x, k'_y \leq 0.05\text{Å}^{-1}$, where the $k.p$ model is valid and these points are colored according to the value of $det(M)$.

Importantly, since $\left|u_{\mathbf{k}'_i}\right\rangle$ is 4-dimentional, we need, at least, four different states in Eq. (G4) to be able to get

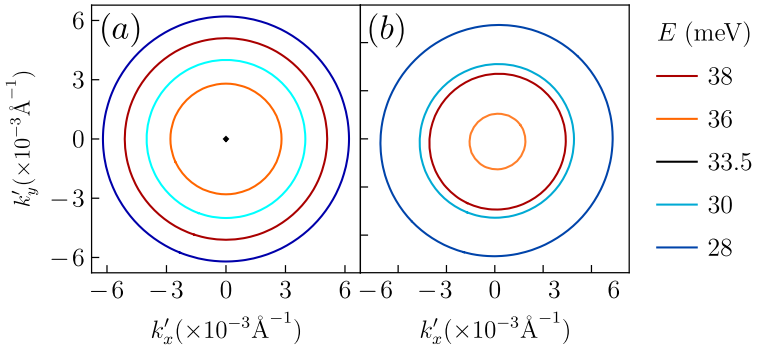

FIG. 7. Energy cuts of the surface states of strained Cd_3As_2 in the (001) surface (a) in the absence of light and (b) in the presence of a CL incident normal to (112). We set the strain type to be B_{1g}, $\omega = 400$ meV and $\mathcal{A}_\prime = 2.4 \times 10^{-2}\text{Å}^{-1}$.

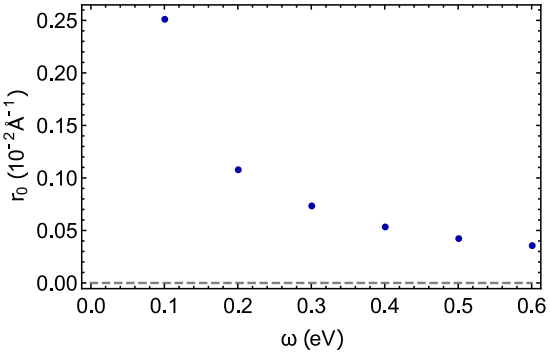

FIG. 8. Position $r_0 = \sqrt{k'^2_x + k'^2_y}$ of the surface Dirac node in the $(1\bar{1}0)$ surface as a function of BCL frequency. We set the incidence direction to be normal to (112) and $\mathcal{A}_0 = 2.6 \times 10^{-2}$ Å^{-1} and $\alpha = \pi/2$.

$\phi(z'=0)=0$. This implies that, in the absence of light, since all the bands are two-fold degenerate, a minimum of two complex k_z' with $\kappa<0$ needs to be found in Eq. (G3). When the light field is included, on the other hand, the degeneracy of the bands is lifted (except at the Weyl nodes) and the minimum number of distinct solutions increases to four.

We applied this technique for semimetallic and the insulating phases of Cd_3As_2. Fig.7 shows cuts of the surface states in Fig.3 of the main text. Fig.8, shows the position of the node of the surface Dirac cone in $(1\bar{1}0)$ surface as a function of the frequency of the BCL. In the latter figure, the parameters are set to be the same as in Fig.4 in the main text.

Appendix H: Temperature dependence of the GME effect

The gyromagnetic effect (GME) describes the current density $\mathbf{J}$ that is induced in a system in response of an slowly-oscillating external magnetic field. This is not an equilibrium current, but rather a low-frequency response of a system that vanishes in insulators and is directly proportional to the energy separation of the Weyl nodes of a non-centrosymmetric Weyl semimetal. In this section, we derive the temperature dependence of the GME effect in Weyl semimetal where the Weyl nodes are separated both in energy and mmentum.

The GME effect is fundamentally different from the chiral magnetic effect (CME) although the form of the induced currents in both effects have similar forms. In contrast to the CME, GME is not governed by a geometric property of the bulk bands. It is the low-frequency limit of natural gyrotropy in non-centrossymetric metals and is governed by the magnetic moment of the Bloch states at the Fermi level [11, 12],

$$\mathbf{J}_i = \alpha_{ij}^{GME} B_j \ , \tag{H1}$$

$$\alpha_{ij}^{GME} = \frac{i\Omega\tau}{1-i\Omega\tau}\sum_{n\in \mathrm{occ}}\int d\mathbf{k}\,\frac{\partial f_{n,\mathbf{k}}}{\partial \varepsilon_{n,\mathbf{k}}} v_{n,\mathbf{k}}^{(i)} m_{n,\mathbf{k}}^{(j)} \ . \tag{H2}$$

Here, $i,j=x,y,z$ denotes Cartesian components, Ω corresponds to the frequency of the magnetic field and τ^{-1} is the electron scattering rate due to disorder. Besides, $f_{n,\mathbf{k}}=\left(\exp\left(\varepsilon_{n,\mathbf{k}}-\mu\right)+1\right)^{-1}$ is the Fermi-Dirac distribution function. $\varepsilon_{n,\mathbf{k}}$ denotes the dispersion of the Bloch bands, whose occupation is controlled by the chemical potential μ. Note that the sum over the band index n runs over the occupied bands only. The other two quantities appearing in the integrand of the GME tensor in Eq.H2 are the band velocity $\mathbf{v}_{n,\mathbf{k}}=(\partial_{\mathbf{k}}\varepsilon_{n,\mathbf{k}})/\hbar$, with $\partial_{\mathbf{k}}\equiv\partial/\partial\mathbf{k}$, and the magnetic moment of a Bloch electron,

$$\mathbf{m}_{n,\mathbf{k}} = \frac{e}{2\hbar}\mathrm{Im}\left\langle \partial_{\mathbf{k}}u_{n,\mathbf{k}}\right| \times \left[\hat{h}(\mathbf{k})-\varepsilon_{n,\mathbf{k}}\right]\left|\partial_{\mathbf{k}}u_{n,\mathbf{k}}\right\rangle \ . \tag{H3}$$

In the expression above, $|u_{n,\mathbf{k}}\rangle$ is the periodic part of the Bloch wave-function, which is the eigenstate of the first-quantized Hamiltonian, $\hat{h}(\mathbf{k})\,|u_{n,\mathbf{k}}\rangle=\varepsilon_{n,\mathbf{k}}\,|u_{n,\mathbf{k}}\rangle$. The expectation value of the spin of the Bloch state also contributes to the the magnetic moment in Eq.(H3) [11], but here, following the approach in Ref. 11 we focus only on its orbital part.

The form of the GME tensor in Eq.(H2) was obtained trough the *uniform limit* of the linear order tensor, $\alpha^{GME}=\lim_{\Omega\to 0}\lim_{q\to 0}\alpha(\mathbf{q},\omega)$. Here, the $\Omega\to 0$ limit means that $\hbar\Omega\ll\epsilon_{inter}$, where ϵ_{inter} is the energy scale associated with interband transitions. For the parameters of Fig.1(a) in the main text, this gives an upper limit of order of GHz for Ω. As we can see from the prefactor in the right-hand side of Eq.(H2), the GME effect is suppressed by disorder and requires $\Omega\tau\gg 1$, which gives a lower bound for Ω.

The expression in Eq.(H2) gets greatly simplified in the case of Weyl semimetal. In the vicinity of a Weyl node, $\varepsilon_{n,\mathbf{k}}=\varepsilon_0-\hbar n v_F k$ and $\mathbf{m}_{n,\mathbf{k}}=-ev_F\chi\mathbf{k}/(2k^2)$, where v_F is the Fermi velocity, χ is the node chirality and $n=\pm 1$. Therefore, for a Fermi surface with pockets coming from two Weyl cones, one with node slightly above the Fermi level and the other slightly below, the GME tensor at $T=0$ takes the well-known form [11]

$$\alpha_{ij}^{(GME)} = \delta_{i,j}\frac{e^2}{3h^2}\Delta E \ , \tag{H4}$$

where ΔE is the energy separation between the the Weyl nodes.

Interestingly, because of the linear dispersion of the Weyl nodes, Eq.(H4) is robust to thermal effects. At finite

temperatures, Eq.(H2) becomes $\alpha_{i,j}^{(GME)} = \delta_{i,j} e^2(\chi_1 R_1 + \chi_2 R_2)/(3h^2)$, where

$$R_j \equiv \frac{1}{T}\int_{-\infty}^{\infty} d\varepsilon \frac{(\varepsilon_{0,j} - \varepsilon)}{4\cosh^2(\frac{\varepsilon-\mu}{2T})} = \varepsilon_{0,j} - \mu \ , \tag{H5}$$

recovering the same expression as in the zero temperature case. This effect will be suppressed when the band dispersion deviates from linear and when a finite bandwidth is taken into account.

[1] J. W. Edington, Electron diffraction in the electron microscope, in *Electron Diffraction in the Electron Microscope* (Springer, 1975) pp. 1–77.

[2] M. N. Ali, Q. Gibson, S. Jeon, B. B. Zhou, A. Yazdani, and R. J. Cava, The crystal and electronic structures of Cd_3As_2, the three-dimensional electronic analogue of graphene, Inorganic chemistry **53**, 4062 (2014).

[3] Z. Wang, H. Weng, Q. Wu, X. Dai, and Z. Fang, Three-dimensional Dirac semimetal and quantum transport in Cd_3As_2, Phys. Rev. B **88**, 125427 (2013).

[4] P. Villar Arribi, J.-X. Zhu, T. Schumann, S. Stemmer, A. A. Burkov, and O. Heinonen, Topological surface states in strained Dirac semimetal thin films, Phys. Rev. B **102**, 155141 (2020).

[5] S. Jeon, B. B. Zhou, A. Gyenis, B. E. Feldman, I. Kimchi, A. C. Potter, Q. D. Gibson, R. J. Cava, A. Vishwanath, and A. Yazdani, Landau quantization and quasiparticle interference in the three-dimensional Dirac semimetal Cd 3 As 2, Nature materials **13**, 851 (2014).

[6] D. Varjas, T. Ö. Rosdahl, and A. R. Akhmerov, Qsymm: Algorithmic symmetry finding and symmetric hamiltonian generation, New Journal of Physics **20**, 093026 (2018).

[7] T. Mikami, S. Kitamura, K. Yasuda, N. Tsuji, T. Oka, and H. Aoki, Brillouin-Wigner theory for high-frequency expansion in periodically driven systems: Application to Floquet topological insulators, Phys. Rev. B **93**, 144307 (2016).

[8] S. Rahav, I. Gilary, and S. Fishman, Effective Hamiltonians for periodically driven systems, Phys. Rev. A **68**, 013820 (2003).

[9] A. Eckardt and E. Anisimovas, High-frequency approximation for periodically driven quantum systems from a floquet-space perspective, New journal of physics **17**, 093039 (2015).

[10] M. Bukov, L. D'Alessio, and A. Polkovnikov, Universal high-frequency behavior of periodically driven systems: from dynamical stabilization to floquet engineering, Advances in Physics **64**, 139 (2015).

[11] S. Zhong, J. E. Moore, and I. Souza, Gyrotropic Magnetic Effect and the Magnetic Moment on the Fermi Surface, Phys. Rev. Lett. **116**, 077201 (2016).

[12] J. Ma and D. A. Pesin, Chiral Magnetic Effect and Natural Optical Activity in Metals with or without Weyl Points, Phys. Rev. B **92**, 235205 (2015).